Atmos. Chem. Phys., 20, 8123–8137, 2020
https://doi.org/10.5194/acp-20-8123-2020

Atmospheric Chemistry and Physics
Open Access
EGU

Temperature effects on optical properties and chemical composition of secondary organic aerosol derived from *n*-dodecane

Junling Li[1,2,4], Weigang Wang[1,2], Kun Li[5,a], Wenyu Zhang[1,2], Chao Peng[1,2], Li Zhou[6], Bo Shi[1,2], Yan Chen[1,2], Mingyuan Liu[1,2], Hong Li[4], and Maofa Ge[1,2,3]

[1]State Key Laboratory for Structural Chemistry of Unstable and Stable Species, Beijing National Laboratory for Molecular Sciences (BNLMS), CAS Research/Education Center for Excellence in Molecular Sciences, Institute of Chemistry, Chinese Academy of Sciences, Beijing 100190, P. R. China
[2]University of Chinese Academy of Sciences, Beijing 100049, P. R. China
[3]Center for Excellence in Regional Atmospheric Environment, Institute of Urban Environment, Chinese Academy of Sciences, Xiamen, 361021, P. R. China
[4]State Key Laboratory of Environmental Criteria and Risk Assessment, Chinese Research Academy of Environmental Sciences, Beijing 100012, P. R. China
[5]Air Quality Research Division, Environment and Climate Change Canada, Toronto, Ontario M3H5T4, Canada
[6]College of Architecture and Environment, Sichuan University, Chengdu, P. R. China
[a]now at: Laboratory of Atmospheric Chemistry, Paul Scherrer Institute (PSI), 5232 Villigen, Switzerland

Correspondence: Weigang Wang (wangwg@iccas.ac.cn)

Received: 31 December 2019 – Discussion started: 13 February 2020
Revised: 14 June 2020 – Accepted: 19 June 2020 – Published: 13 July 2020

Abstract. Environmental temperature plays a vital role in controlling chemical transformations that lead to the formation of secondary organic aerosol (SOA) and ultimately impact the composition and optical properties of the aerosol particles. In this study, we investigated optical properties of *n*-dodecane SOA under two temperature conditions: 5 and 25 °C. It was shown that low-temperature conditions could enhance the real part of the refractive index (RI) of the SOA at wavelengths of 532 and 375 nm. Mass spectrometry analysis revealed that the molecular composition of *n*-dodecane SOA was significantly modified by temperature: a large amount of oligomers were formed under low-temperature conditions, which led to higher RI values. These findings will help improve our understanding of the chemical composition and optical properties of SOA under different temperature conditions and will provide one possible explanation for the low visibility in suburban areas during winter.

1 Introduction

Organic aerosol, especially secondary organic aerosol (SOA), plays a vital role in air quality, climate change and human health (Kanakidou et al., 2005; Poschl, 2005; Mellouki et al., 2015; Poschl and Shiraiwa, 2015; von Schneidemesser et al., 2015; Shrivastava et al., 2017). SOA accounts for a high proportion of atmospheric particulate matter around the world, especially in heavily polluted areas (Liu et al., 2017; Sun et al., 2014; Huang et al., 2014). Due to the variety of precursors and oxidation pathways, the composition of SOA is very complicated and variable (Lu, 2018; von Schneidemesser et al., 2015; Poschl and Shiraiwa, 2015; Hallquist et al., 2009; George et al., 2015), and the optical properties of SOA also exhibit different characteristics (Shrivastava et al., 2017; Zhang et al., 2015; Moise et al., 2015; Laskin et al., 2015). The complex refractive index (RI), $m = n + ki$ (n is the real part, and k is the imaginary part; they express the extent of scattering and absorbing, respectively), is the only intrinsic optical property of a particle. The RI is controlled by the chemical composition and physi-

cal characteristics (e.g., morphology and shape) of a particle (Moise et al., 2015). Quantifying the RI of aerosol particles is highly important to evaluate their optical properties and to further estimate their impacts on atmospheric visibility and the Earth's radiative balance.

Aerosol physicochemical properties are strongly dependent on the atmospheric conditions, such as the relative humidity (Ervens et al., 2011; Sun et al., 2014), temperature (Wang et al., 2017) and oxidizing conditions, the latter of which includes the oxidant type, e.g., NO_3, OH and O_3, and the oxidation concentrations, e.g., photochemical age (Cheng et al., 2016; Shrivastava et al., 2017; George et al., 2015; Kanakidou et al., 2005). Therefore, it is important to study SOA formation and optical properties under varying atmospheric conditions to simulate the processes in the real atmosphere. There have been a number of smog chamber experiments on the effect of seed particles (Huang et al., 2017; Denjean et al., 2014; Song et al., 2013; Lee et al., 2013; Li et al., 2017a, 2018; Trainic et al., 2011); oxidant type, e.g., NO_3 (Peng et al., 2018; Lu et al., 2011; OH, Liu et al., 2015; Lin et al., 2015; Li et al., 2014; Nakayama et al., 2013; Cappa et al., 2011) and O_3 (Peng et al., 2018; Kim et al., 2014; Flores et al., 2014; Kim and Paulson, 2013); oxidation concentrations, e.g., photochemical age (Zhong and Jang, 2014; Kim et al., 2014; Lambe et al., 2012, 2013); and relative humidity (RH; Titos et al., 2016; McNeill, 2015; Denjean et al., 2015; Li et al., 2017b; Sareen et al., 2017; Ye et al., 2016; Michel Flores et al., 2012) on SOA formation and the RI values of SOA derived from both biogenic and anthropogenic volatile organic compounds (VOCs). There have also been many studies investigating temperature effects on SOA formation and composition (Takekawa et al., 2003; Svendby et al., 2008; Clark et al., 2016; Lamkaddam et al., 2016; Huang et al., 2018; Mu et al., 2018; Zhao et al., 2019; Boyd et al., 2017; Price et al., 2016; Emanuelsson et al., 2013; Warren et al., 2009; Qi et al., 2010); however, works on the effect of temperature on the SOA RI are limited (Kim et al., 2014). Field studies have shown that temperature is an important factor affecting the rate constants of the oxidation process, the vapor pressure of products, and SOA formation process and yields (Atkinson and Arey, 2003; Wang et al., 2017; Roy and Choi, 2017; Ding et al., 2017; Cui et al., 2016). Therefore, investigating temperature dependence is important to develop a better understanding of the formation and the physical and chemical properties of SOA under tropospheric conditions.

Long-chain alkanes, which are an important class of intermediate-volatility organic compounds (IVOCs; Zhao et al., 2014) and a large fraction of diesel fuel and its exhaust (Gentner et al., 2012, 2017), are an important potential contributor of SOA (Presto et al., 2009; Zhao et al., 2016). Several previous studies have reported the formation of SOA derived from long-chain alkanes under various conditions, including SOA compositions (Fahnestock et al., 2015; Hunter et al., 2014; Lim and Ziemann, 2005), SOA yields (Loza et al., 2014; Lim and Ziemann, 2009a) and the chemical mechanisms (Yee et al., 2012, 2013; Aimanant and Ziemann, 2013; Lim and Ziemann, 2009b). Recently, Lamkaddam et al. (2016) reported the temperature dependence (10, 20 and 31.5°) of SOA formation from high-NO_x photooxidation of *n*-dodecane and found that temperature did not significantly influence SOA yield. They attributed this to two possible reasons: the changes in reaction rate constants lead to different SOA compositions, or the SOA formed is mainly comprised of nonvolatile compounds and is, therefore, not sensitive to temperature. Li et al. (2017a) reported the optical properties of SOA from *n*-dodecane, *n*-pentadecane and *n*-heptadecane under various oxidation conditions at room temperature. However, knowledge on the effect of temperature on the chemical composition and optical properties of *n*-dodecane SOA in the absence of NO_x is still lacking, which limits our understanding of the role of SOA in visibility and the radiative balance under different temperature conditions (e.g., in winter and summer).

In the present study, we determined the temperature effects on the chemical composition and optical properties of SOA generated in a smog chamber during the photooxidation of *n*-dodecane under low-NO_x conditions. These results will improve our understanding of the impact of temperature on SOA chemical compositions and optical properties and, in turn, on air quality and radiative forcing.

2 Materials and methods

2.1 Smog chamber experiments

The experiments were performed in a dual-reactor smog chamber, the details of which are given in Wang et al. (2015). Briefly, the chamber consisted of two 5 m^3 reactors made of fluorinated ethylene propylene (FEP) Teflon film, which were housed in a thermally isolated enclosure. The temperature in the chamber was accurately controlled by a high-power air conditioner within the range from −10 to 40 °C. Multiple light sources were used in the chamber, with a center wavelength of 365 nm (GE, F40BL), 340 nm (Q-lab, UVA-340) and 254 nm (PHILIPS, G36 T8). The RH and temperature in the chamber were continuously monitored and controlled throughout the experiments. The experiments were conducted at an RH $< 5\,\%$ and under two different temperature conditions: 25 °C (room temperature, *R*) and 5 °C (low temperature, *L*). The temperature fluctuation was ±0.5 °C for both conditions. As the optical properties of the SOA can be affected by many factors, other factors had to remain unchanged in order to study the impact of temperature; thus, the humidity of the experiments was constant and could not be changed. Here, the experiments were conducted under dry conditions. This was due to the fact that when the temperature changed, the saturated vapor pressure of water changed: if the RH was consistent at different temperatures, the con-

centration of the water was not consistent; when the concentration of water was the same, the RH was different. Therefore, choosing different humidity (non-dry) conditions would introduce new problems, and we could only use dry conditions (RH < 5 %). The *n*-dodecane (≥ 99 %, Sigma-Aldrich) was photooxidized under low-NO_x conditions, with hydrogen peroxide (30 % wt/wt, Beijing Chemical Works) as the OH precursor. *n*-Dodecane was added into the chamber first and was followed by hydrogen peroxide. The wind turbine was then turned on for 20 min to ensure that the materials in the chamber were well mixed.

When all of the substances were added to the chamber, the chamber was set to the desired temperature. The instruments were connected at room temperature, and when the temperature dropped to 5° and stabilized, the data measured by the instruments were considered to be valid data. The lights in the chamber were then turned on, and the photooxidation reaction started. The initial conditions for these experiments are listed in Table 1. According to our experimental design, the expected concentration of *n*-dodecane was 50 ppb, which involved introducing 2 µL of liquid *n*-dodecane into the 5 m^3 smog chamber. As the injection volume of *n*-dodecane was 2 µL, volume error during injection was inevitable, which would influence the concentration of *n*-dodecane in the chamber. Nevertheless, the relatively small differences in the *n*-dodecane concentration (43–50 ppb at low temperature and 52–58 ppb at high temperature) likely had little influence on the SOA composition and optical properties.

2.2 Measurements

All instruments were located within 1 m of the chamber, and all of the connection tubes were wrapped with insulation cotton to minimize the influence of room temperature. The concentration of NO_x and the O_3 formed in the smog chamber were monitored using gas analyzers (Teledyne Advanced Pollution Instrumentation, Model T400 and Model T200UP, respectively). The concentration of *n*-dodecane was monitored using a proton transfer reaction quadrupole mass spectrometer (PTR-QMS 500, IONICON), and calibration of the response of the PTR-QMS to *n*-dodecane was achieved through permeation tubes. The NO^+ ion source of the PTR-QMS was used when detecting the *n*-dodecane (Koss et al., 2016; Shi et al., 2019; Paulsen et al., 2005).

The particle size distribution and density were detected by a scanning mobility particle sizer (SMPS, TSI) and a centrifugal particle mass analyzer (CPMA, Cambustion). A custom-made cavity ring-down spectrometer (CRDS; Wang et al., 2012) was applied to monitor the optical properties of the formed particles at 532 nm. A photoacoustic extinctiometer (PAX-375, Droplet Measurement Technologies) was used to measure the scattering, absorption and extinction coefficients of formed SOA at 375 nm.

The optical properties of the formed particles were analyzed after the mass concentration of the aerosol reached a maximum. During the following 1–2 h, the surface mean diameter and the extinction coefficients of the particles tended to be stable and did not change much. We then collected the particles on the film to analyze their chemical composition during the same period. The sample collection time was chosen to make sure that the signal of the collection filter was much higher than the background of the blank filter in mass spectrometry. Another principle is to reduce the sample volume consumed during sampling. If the membrane extraction time is too long, the chamber volume will decrease too much. The formed aerosol particles were collected on the PTFE (polytetrafluoroethylene) membrane that had a pore size of 200 nm (0.2 µm, 47 mm, Merck Millipore FELP). Each filter sample was collected for 30 min at a 10 L min^{-1} flow rate. The filters were then put into 5 mL of methanol (99.9 %, Fisher Chemical) and sonicated for 30 min. The dissolved solution was analyzed with a UV–Vis light spectrometer (Avantes 2048F), which was used to detect the absorbing properties (to derive the imaginary part of RI, *k*) at 532 nm. The solution was also analyzed using electrospray ionization time-of-flight mass spectrometry (ESI-ToF-MS, Bruker, Impact HD) to obtain the chemical composition of the formed SOA. Positive ion mode was used for the ESI-ToF-MS. The absolute mass error was below 3 ppm, and the typical mass resolving power was > 30 000 at m/z 200.

2.3 Calculation method of RI values

2.3.1 Calculation method of RI values based on the CRDS

The RI values of the particles formed in the smog chamber were estimated based on both the extinction and scattering coefficients and Mie–Lorenz theory (Bohren and Huffman, 1983). The details of the RI values' calculation method are also reported in our previous publications (Wang et al., 2012; Phillips and Smith, 2014; Li et al., 2017a, b, 2018; Peng et al., 2018).

The extinction coefficients (α_{ext}) of the particles established using CRDS can be calculated with Eq. (1):

$$\alpha_{ext} = \frac{L}{cl}\left(\frac{1}{\tau} - \frac{1}{\tau_0}\right), \quad (1)$$

where L is the distance between the two mirrors in the cavity, l is the length of the cavity that filled with aerosol particles, c is the speed of the light, τ_0 is the ring-down time of the CRDS when it is filled with zero air and τ is the ring-down time of the CRDS when it is filled with aerosol particles.

For the homogeneous spherical particles, the α_{ext} can be calculated using Eq. (2):

$$\alpha_{ext} = N\sigma_{ext} = \frac{1}{4}N\pi D^2 Q_{ext}, \quad (2)$$

Table 1. The initial conditions of the smog chamber experiments.

Experiment no.[a]	HC (ppb)	H_2O_2 (ppm)	NO_x (ppb)	RH (%)	Temperature (°C)	Mass[b] ($\mu g\,m^{-3}$)	Mass[c] ($\mu g\,m^{-3}$)
Dod-R-1	58	1.03	< 1	< 5	25	155	225
Dod-R-2	52	1.03	< 1	< 5	25	135	197
Dod-L-1	43	1.07	< 1	< 5	5	128	342
Dod-L-2	50	1.09	< 1	< 5	5	133	387

[a] Experimental conditions: *n*-dodecane at room temperature (Dod-R) and *n*-dodecane at low temperature (Dod-L). [b] The mass concentration is obtained without wall loss correction. [c] The mass concentration is calculated with wall loss correction.

where N is the concentration of the spherical particles, σ_{ext} is the extinction cross section, D is the particle diameter and Q_{ext} is the extinction efficiency.

Q_{ext} is the ratio of the Beer's law extinction cross section to the geometric area of the spherical particles; it is dimensionless, and can be expressed using Eq. (3):

$$Q_{ext} = \frac{4\alpha_{ext}}{N\pi D^2} \tag{3}$$

For the polydisperse SOA particles formed in the smog chamber, which follow a log-normal distribution and have a geometric standard deviation that is always smaller than 1.5, the Q_{ext} with a surface mean diameter of D_s can be expressed as follows (with the assumption that the aerosol particles in each size bin are homogeneous spherical particles; Nakayama et al., 2010):

$$Q_{ext}(D_s) = \frac{\alpha_{ext}}{\int N\left(D_p\right)\frac{1}{4}\pi D_p^2 \mathrm{d}D_p}, \tag{4}$$

where D_p is the geometrical diameter of the particle, $\mathrm{d}D_p$ is the size bin of the particles and $N(D_p)$ is the number concentration of the particles in $\mathrm{d}D_p$ with D_p per unit volume.

For the particles with D_p in each size bin $\mathrm{d}D_p$, the surface area $S(D_p)$can be expressed by Eq. (5):

$$S(D_P) = N\left(D_p\right)\pi D_p^2 \tag{5}$$

Thus, Eq. (4) can also be expressed as follows:

$$Q_{ext}\left(D_s\right) = \frac{\alpha_{ext}}{\int \frac{1}{4}S(D_p)\mathrm{d}D_p} = \frac{4\alpha_{ext}}{S_{tot}}, \tag{6}$$

where S_{tot} is the total surface area of the particles, and the values can be obtained with an SMPS.

The extinction efficiency can also be calculated with Mie–Lorenz theory:

$$Q_{ext}(D_s) = \int f\left(D_p\right) Q_{ext}(D_p)\mathrm{d}D_p, \tag{7}$$

where $f(D_p)$ is the normalized surface area-weighted size distribution function. The measured extinction efficiency ($Q_{ext,mea}$) is then compared to the calculated extinction efficiency ($Q_{ext,cal}$), and the best-fit RI value is determined by minimizing the following reduced merit function (χ_r):

$$\chi_r = \frac{1}{N}\sum_{i=1}^{N}\left(Q_{ext,mea} - Q_{ext,cal}(n,k)\right)_i^2, \tag{8}$$

where N is the number of diameters to be calculated.

The uncertainties of the particle concentration and the surface mean diameter measured by SMPS are ±10 % and ±1 %, respectively. The uncertainty of the retrieval method is ±0.002, and the uncertainty of the measured extinction coefficient with CRDS is ±3 %, resulting in a final uncertainty of the retrieved RI value of about 0.02–0.03. The corresponding equation for the RI value uncertainty is given in the Supplement.

2.3.2 Calculation method of RI values based on the quantitative structure–property relationship (QSPR)

Using the molecular formula obtained from ESI-ToF-MS, we calculated the RI values of the products in SOA with the quantitative structure–property relationship (QSPR) method (Redmond and Thompson, 2011). The QSPR can be expressed as follows:

$$\mathrm{RI}_{predicted} = 0.031717\,(\mu) + 0.0006087\,(\alpha) - 3.0227\left(\frac{\rho_m}{M}\right) + 1.38709, \tag{9}$$

where μ is the unsaturation of the molecular formula, α is the polarizability of the molecular formula, ρ_m is the mass density ($g\,cm^{-3}$) and M is the molar mass ($g\,mol^{-1}$).

The mass density of the compound is estimated using the AIM (Aerosol Inorganics Model), the details of which are given in Girolami (1994).

μ is calculated via the conventional approach, which is used in many organic chemistry texts:

$$\mu = (\mathrm{no.\,C} + 1) - 0.5(\mathrm{no.\,H} - \mathrm{no.\,N}), \tag{10}$$

where no. C, no. H and no. N are the number of the C, H and N, respectively.

α is calculated based on the molecular formula of the compound, and it can be expressed as follows:

$$\alpha = 1.51\,(\text{no. C}) + 0.17\,(\text{no. H}) + 0.57\,(\text{no. O}) + 1.05\,(\text{no. N}) + 2.99\,(\text{no. S}) + 2.48\,(\text{no. P}) + 0.22\,(\text{no. F}) + 2.16\,(\text{no. Cl}) + 3.29(\text{no. Br}) + 5.45(\text{no. I}) + 0.32, \quad (11)$$

where "no." is the number of the atoms of each element in the molecular formula.

The calculated RI values of products were used to link the chemical composition and optical properties as well as to explain the observed RI differences at different temperatures in Sect. 3.4.

2.3.3 Calculation method of average elemental composition and ratios

Due to the complexity of the chemical composition in SOA particles, it is common to express the bulk composition as averaged elemental ratios. The average elemental composition and ratios (C, H, O, H/C and O/C) can be estimated from the identified molecular formulas (Ervens et al., 2011):

$$\langle Y \rangle = \frac{\sum_i x_i Y_i}{\sum_i x_i} \quad (12)$$

$$\langle Y/Z \rangle = \frac{\sum_i x_i Y_i}{\sum_i x_i Z_i}, \quad (13)$$

where $Y = \text{C, H, O}$, $Y/Z = \text{H/C, O/C}$. Here, x_i is the peak abundance of the elemental composition.

2.4 Impact of temperature on direct radiative forcing

The simple forcing efficiency (SFE) is used to determine the relative importance of the optical properties of the aerosol to direct radiative forcing at the Earth's surface (Bond and Bergstrom, 2006):

$$\text{SFE} = \frac{S_0}{4}\tau_{\text{atm}}^2\,(1 - F_{\text{c}})\left[2(1-a_{\text{s}})^2\frac{Q_{\text{bs}}C}{M} - 4a_{\text{s}}\frac{Q_{\text{a}}C}{M}\right], \quad (14)$$

where S_0 is the solar radiation, τ_{atm} is the transmission of the atmosphere, F_{c} is the cloud fraction, a_{s} is the surface albedo, Q_{bs} and Q_{a} are the backscattering and absorption efficiency of the aerosol particles, M is the aerosol mass, and C is the cross section of the aerosol.

The SOA derived from n-dodecane has negligible absorption at the wavelengths of 532 and 375 nm under the two temperature conditions; thus, the value of Q_{a} is zero, and the impact of temperature on the direct radiative forcing (DRF) can be expressed using

$$\text{DRF ratio} = \frac{\text{SFE}_{\text{low temperature}}}{\text{SFE}_{\text{normal temperature}}} = \frac{Q_{\text{bs, low tem.}}}{Q_{\text{bs, normal tem.}}}, \quad (15)$$

and this will be discussed Sect. 3.5.

3 Results and discussion

3.1 Photooxidation experiments

The profiles of the n-dodecane photooxidation experiments at different temperatures are shown in Fig. S1 in the Supplement. As similar amounts of n-dodecane and oxidant were added to the smog chamber and the reaction rate was lower under low temperature, the reaction time under low-temperature conditions was significantly longer than that at room temperature: 4–5 h for room temperature and 8–9 h for low-temperature conditions. Under room temperature conditions, the total surface concentration and mass reached a maximum after 3 h, whereas it reached a maximum after 6 h under low-temperature conditions.

3.2 The effect of temperature on RI

The optical properties of the formed particles were analyzed after the mass concentration of the aerosol reached a maximum, and data from the last 1 h were used. During this period, the surface mean diameter and the extinction coefficients (α_{ext}) of the particles tended to be stable and did not change much. The extinction coefficients and the extinction efficiency of the particles as a function of the surface mean diameter are shown in Fig. S4 in the Supplement. The SOA derived from n-dodecane had no significant absorption at 532 or 375 nm, similar to our previous study (Li et al., 2017a), and the imaginary part of the RI will not be discussed here. The real part of the RI obtained in this study is shown in Fig. 1. As shown in Fig. 1, the RI values at 532 nm at room temperature were similar to our previous study (Li et al., 2017a), whereas the two temperature conditions had significantly different RI ranges: 1.472–1.486 (25 °C) and 1.502–1.526 (5 °C) at 532 nm; 1.51–1.53 (25 °C) and 1.532–1.56 (5 °C) at 375 nm. Details on the variation tendency of the RI values as a function of the surface mean diameter for SOA produced under room temperature and low-temperature conditions are given in Fig. 2. The various RI values at different temperatures indicate that lower reaction temperatures (from 25 to 5 °C) had an enhancing effect (~ 0.03 at 532 nm and ~ 0.02 at 375 nm) on the RI of n-dodecane SOA. The mass spectrometry analysis below (Sect. 3.3) was applied to obtain chemical composition information and explain the phenomenon above.

3.3 Temperature effect on the chemical composition and reaction mechanism

The higher RI values under low-temperature conditions indicated that the temperature might change the chemical composition of SOA by changing the reaction types or shifting the balance of different pathways. The mass spectra (MS) of n-dodecane SOA obtained by ESI-ToF-MS in positive ion mode are shown in Fig. 3, and they provide molecular insight into the chemical changes under different temperature condi-

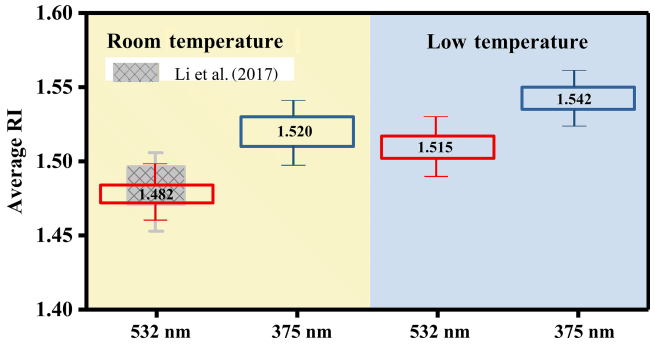

Figure 1. Summary of the averaged RI values of *n*-dodecane SOA at room temperature (25 °C; the light orange area) and under low-temperature conditions (5 °C; the light blue area) at wavelengths of 532 and 375 nm. The red box is the averaged RI value for *n*-dodecane at 532 nm, the shaded boxes are the RI values from our previous study at 532 nm (Li et al., 2017a) and the blue box is the averaged RI value for *n*-dodecane at 375 nm.

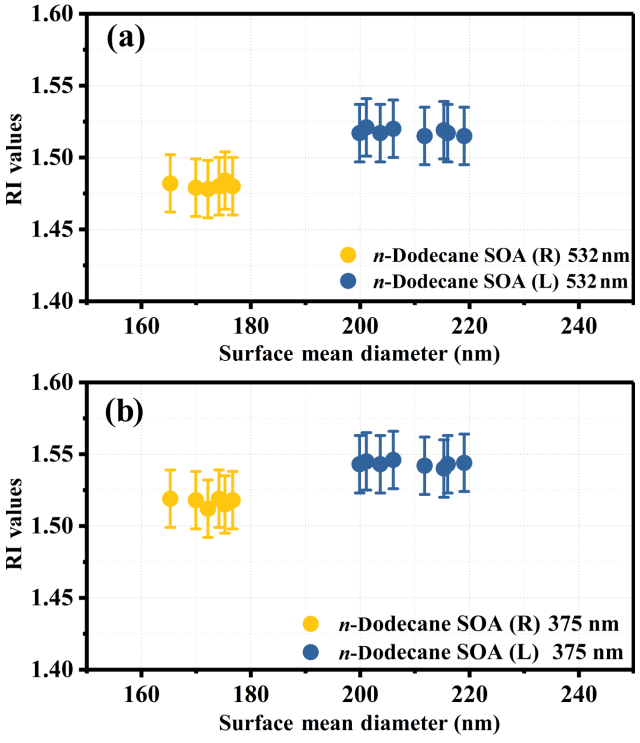

Figure 2. Variation tendency of the RI values as a function of the surface mean diameter for SOA produced at room temperature and under low-temperature conditions at **(a)** 532 nm and **(b)** 375 nm.

tions. We identified about 260 individual masses for SOA under the two temperature conditions, and details are given in Fig. S2 and Table S1 in the Supplement. The spectrum under low-temperature conditions was significantly different from the spectrum at room temperature, with a large amount of ions corresponding to monomer, dimer, trimer and tetramer.

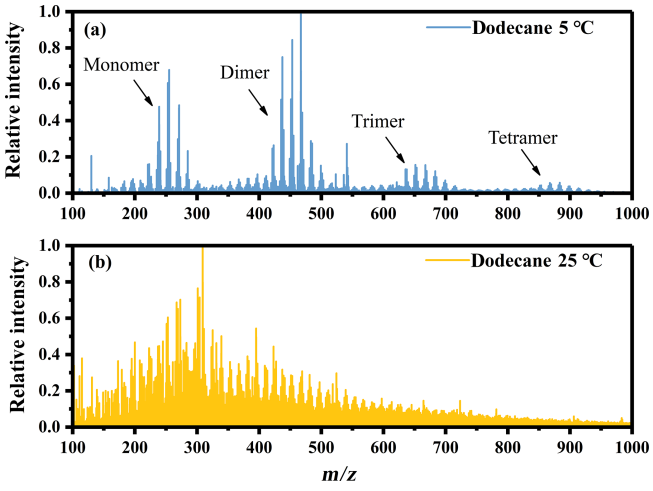

Figure 3. Mass spectra of *n*-dodecane SOA obtained by ESI-ToF-MS in positive ion mode. **(a)** Low-temperature conditions and **(b)** room temperature conditions.

This suggests that oligomerization might play a dominant role under low-temperature conditions.

The molecular composition of *n*-dodecane SOA was significantly modified by temperature conditions, with the averaging SOA formula changing from $C_{14.98}H_{26.47}O_{5.53}$ at room temperature to $C_{21.25}H_{40.44}O_{7.43}$ under low-temperature conditions. The average carbon number increased from 14.98 at room temperature to 21.25 under low-temperature conditions, indicating that the SOA molecules were larger at lower temperatures. The average O/C and H/C ratios at room temperature were 0.37 and 1.72, respectively, whereas the ratios were 0.35 and 1.90 under low-temperature conditions, respectively. The products formed under low-temperature conditions tended to have a higher H/C ratio and a lower O/C ratio compared with the products formed at room temperature. The details on the O/C and H/C ratios of the products formed under different temperature conditions can be found in Fig. 5a. The phenomenon above might be due to the presence of oligomers.

For the oligomers in the mass spectrum, one possible explanation was that low-temperature conditions promoted gas–particle partitioning and changed the particle-phase reaction. Gas-phase OH oxidation could reduce the H/C ratios and increase the O/C ratios (Li et al., 2018, 2019; Lambe et al., 2015), whereas particle-phase oligomerization basically could not change the O/C or H/C ratios (Charron et al., 2019). At room temperature, more gas-phase oxidation steps were needed to cause the less volatile products to condense into the particle phase (due to the high temperature, i.e., high saturation vapor pressure). Hence, products formed at room temperature had lower H/C and higher O/C ratios. In contrast, the more volatile (i.e., less oxidized) products were readily condensed into the particle phase under low-temperature conditions and then subse-

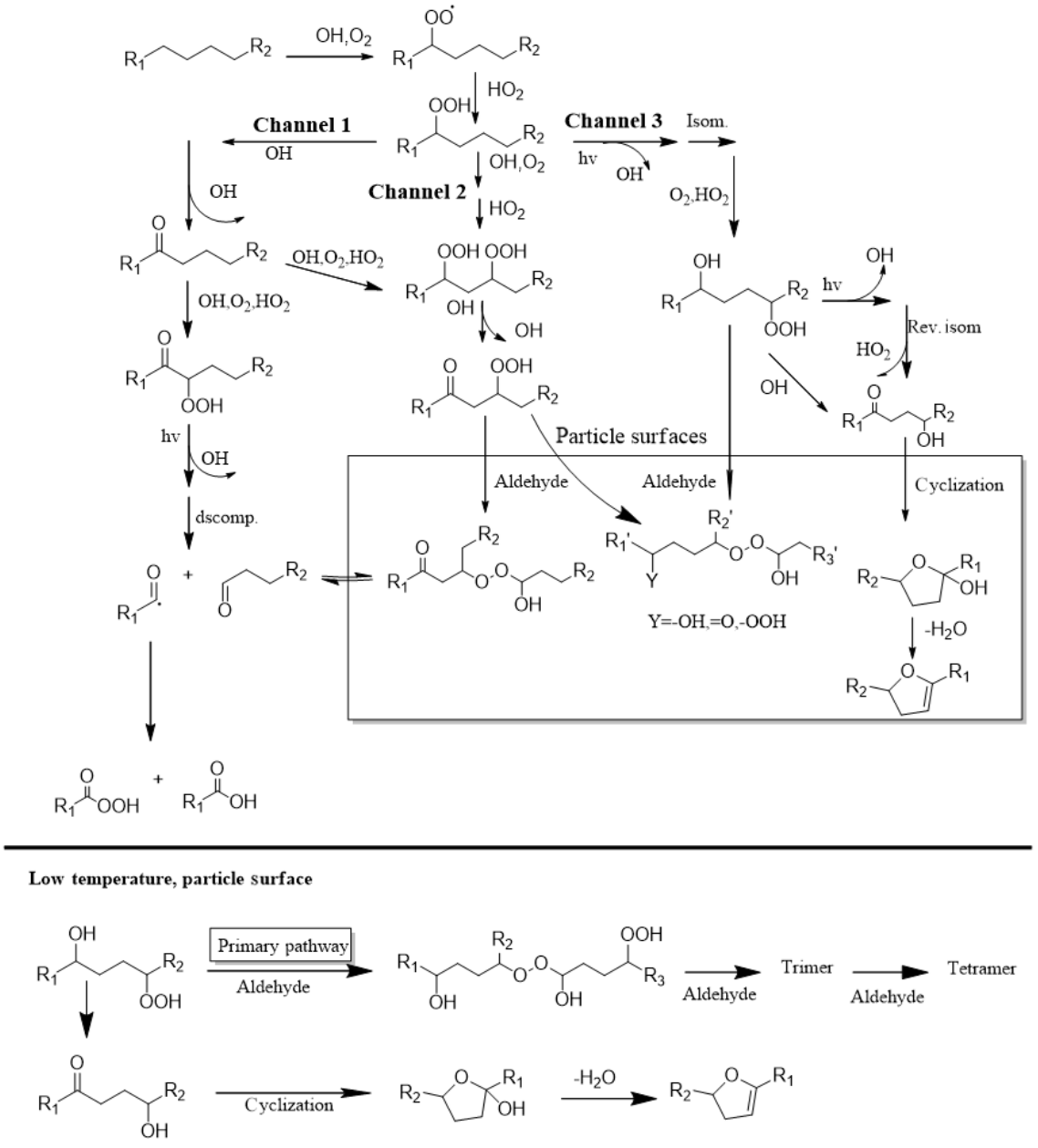

Figure 4. The proposed reaction mechanism of long-chain alkanes under low-NO_x conditions (Fahnestock et al., 2015; Yee et al., 2013, 2012).

quently underwent particle-phase reactions, e.g., oligomerization, leading to the formation of products with higher H/C and lower O/C ratios. This phenomenon was consistent with Kim et al. (2014), who studied the dependence of real part of the RI on the O/C and H/C ratios of SOA derived from limonene and α-pinene and found that the higher percentage of less oxygenated semivolatile substances was responsible for the higher RI values.

For particle-phase reactions, there were two main reaction pathways (Fahnestock et al., 2015; Yee et al., 2012, 2013): intramolecular cyclization of multifunctional hydroperoxides (which form furan derivatives) and intermolecular oligomerization of multifunctional hydroperoxides with aldehydes (which form peroxyhemiacetal, PHA). These two pathways were competitive during the particle-phase reaction process. Based on the mass spectra analysis, we speculated that low temperature promoted the progress of the oligomerization reaction and made it the primary pathway in the particle phase, as shown in Fig. 4. As discussed above, products with a higher volatility and lower oxidation state would condense into the particle phase under low-temperature conditions and

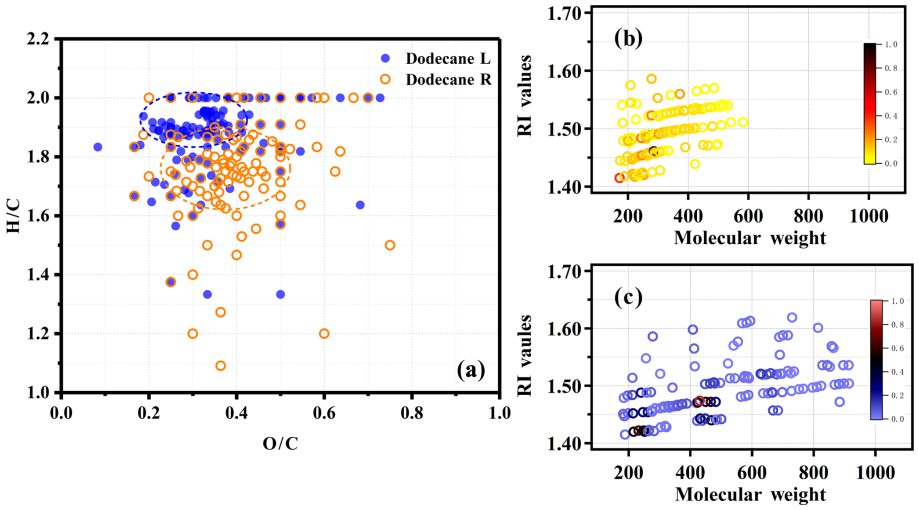

Figure 5. Panel **(a)** shows a van Krevelen plot of the O/C and H/C ratios for identified products from EST-ToF-MS. The orange circle is for the SOA generated at room temperature, and the blue circle is for the SOA generated under low-temperature conditions. Panels **(b)** and **(c)** show the calculated RI values of the selected identified molecular species from MS spectra at room temperature and under low-temperature conditions, respectively; the color maps refer to the relative intensity of the molecular formula.

subsequently participate in particle-phase reactions, which would further promote the oligomerization reaction.

Another possible explanation was that the pathway of the gas-phase reaction changed under low-temperature conditions compared with room temperature conditions. Combining existing mass spectrometry information, we speculated that the oligomers might also be formed by gas-phase radical oligomerization under low-temperature conditions and then rapidly deposited into the particle phase. However, these are speculations based on the existing analysis results. The specific reaction mechanism under low-temperature condition requires further investigation.

Clark et al. (2016) found that the SOA formed from isoprene had similar mass spectra in the monomer range at different temperatures. However, the precursors are very different (isoprene vs. *n*-dodecane) and have very different oxidation pathways and partitioning processes. Hence, it is possible that we observe different results in mass spectra in the monomer range. As mentioned above, the different oxidation degree and partitioning process caused the difference in the monomer range. At room temperature, more OH oxidation steps in the gas phase can lead to the formation of some fragmentation products that may not be observed at low temperatures. For example, we observed the high intensity of m/z 195 $C_{10}H_{20}O_2$ (relative intensity 0.39) and m/z 211 $C_{10}H_{20}O_3$ (relative intensity 0.13) at room temperature but very low intensity (0.012 and 0.041, respectively) at low temperature; furthermore, m/z 195 and m/z 211 are likely products of gas-phase OH oxidation. This process may be different from isoprene (Clark et al., 2016). This is due to the fact that the carbon number is high, volatility is low and fewer oxidation steps are needed before partitioning for *n*-dodecane, whereas there are only five carbon atoms for isoprene so more oxidation steps are needed before partitioning regardless of temperature. Overall, the differences in the monomer range still make sense.

3.4 Relationship between RI values and the chemical composition of SOA

The RI of aerosol particles is fundamentally the results of a combination of particle chemical compositions and internal mixing. SOA particles formed in the smog chamber are treated as homogenous mixtures, and the RI values of these mixtures can be expressed as follows (Redmond and Thompson, 2011):

$$\mathrm{RI} = \sum x_i \mathrm{RI}_i, \tag{16}$$

where x_i is the fraction of the ith component, and RI_i is the refractive index of component i.

The RI values were calculated for the identified products (with high intensity) at room temperature and under low-temperature conditions (details are given in Fig. 5b and c and in Table S1 in the Supplement). It can clearly be seen that the RI values of the products at room temperature were mainly in the range of 1.4 to 1.5, and the degree of oligomerization was generally in the monomer to dimer range. However, for the products formed under low-temperature conditions, the RI values were within the range of 1.4 to 1.55, and the degree of oligomerization could reach tetramerization. As the degree of oligomerization increased, the RI also gradually increased. This generally explained the higher RI of SOA under lower-temperature conditions.

To further validate our speculation and identify the relationship between the measured RI values and the chemical

Table 2. The calculated RI values for the surrogate system: oligomers (11 types of PHA) and furan derivatives.

Molecular formula	Molecular weight	Polarizability	Unsaturation	Predicted RI
$C_{12}H_{26}O_3$	218.32	24.57	0	1.39017
$C_{12}H_{24}O_3$	216.31	24.23	1	1.42236
$C_{12}H_{22}O_4$	230.29	24.46	2	1.45422
$C_{12}H_{24}O_4$	232.31	24.8	1	1.42203
$C_{12}H_{22}O_5$	246.29	25.03	2	1.45389
$C_{12}H_{24}O_5$	248.3	25.37	1	1.42174
$C_{12}H_{20}O_5$	244.27	24.69	3	1.48607
$C_{12}H_{18}O_6$	258.26	24.92	4	1.51681
$C_{12}H_{20}O_6$	260.27	25.26	3	1.48574
$C_{12}H_{24}O_6$	264.3	25.94	1	1.4215
$C_{12}H_{22}O_6$	262.29	25.6	2	1.4536
$C_{22}H_{44}O_6$	404.56	44.44	1	1.43921
$C_{22}H_{46}O_6$	406.58	44.78	0	1.40724
$C_{22}H_{42}O_7$	418.54	44.67	2	1.47106
$C_{22}H_{44}O_7$	420.56	45.01	1	1.43909
$C_{22}H_{42}O_8$	434.54	45.24	2	1.47095
$C_{22}H_{44}O_8$	436.56	45.58	1	1.43899
$C_{22}H_{40}O_8$	432.53	44.9	3	1.50292
$C_{22}H_{38}O_9$	446.51	45.13	4	1.53478
$C_{22}H_{40}O_9$	448.53	45.47	3	1.50281
$C_{22}H_{44}O_9$	452.56	46.15	1	1.43948
$C_{22}H_{42}O_9$	450.54	45.81	2	1.47085
$C_{32}H_{64}O_9$	592.82	64.65	1	1.45319
$C_{32}H_{66}O_9$	594.83	64.99	0	1.42134
$C_{32}H_{62}O_{10}$	606.8	64.88	2	1.48505
$C_{32}H_{64}O_{10}$	608.82	65.22	1	1.4532
$C_{32}H_{62}O_{11}$	622.8	65.45	2	1.48505
$C_{32}H_{64}O_{11}$	624.81	65.79	1	1.45361
$C_{32}H_{60}O_{11}$	620.78	65.11	3	1.5169
$C_{32}H_{58}O_{12}$	634.77	65.34	4	1.54876
$C_{32}H_{60}O_{12}$	637.78	65.68	3	1.51691
$C_{32}H_{64}O_{12}$	640.81	66.36	1	1.45403
$C_{32}H_{62}O_{12}$	638.8	66.02	2	1.48547
$C_{42}H_{84}O_{12}$	781.07	84.86	1	1.46637
$C_{42}H_{86}O_{12}$	783.09	85.2	0	1.4349
$C_{42}H_{82}O_{13}$	795.05	85.09	2	1.49823
$C_{42}H_{84}O_{13}$	797.07	85.43	1	1.46676
$C_{42}H_{82}O_{14}$	811.05	85.66	2	1.49861
$C_{42}H_{84}O_{14}$	813.07	86	1	1.46715
$C_{42}H_{80}O_{14}$	809.04	85.32	3	1.53008
$C_{42}H_{78}O_{15}$	823.02	85.55	4	1.56194
$C_{42}H_{80}O_{15}$	825.04	85.89	3	1.53047
$C_{42}H_{84}O_{15}$	829.07	86.57	1	1.46753
$C_{42}H_{82}O_{15}$	827.05	86.23	2	1.499
$C_{12}H_{23}O_2$	199.3	23.49	1.5	1.43592
$C_{12}H_{21}O_3$	213.28	23.72	2.5	1.46778
$C_{12}H_{23}O_3$	215.3	24.06	1.5	1.43562
$C_{12}H_{22}O_3$	214.29	23.89	2	1.45228
$C_{12}H_{21}O_4$	229.28	24.29	2.5	1.46748
$C_{12}H_{20}O_4$	228.27	24.12	3	1.48413
$C_{12}H_{22}O_4$	230.29	24.46	2	1.45198
$C_{12}H_{19}O_4$	227.27	23.95	3.5	1.49964
$C_{12}H_{17}O_5$	241.25	24.18	4.5	1.5315
$C_{12}H_{19}O_5$	243.27	24.52	3.5	1.49934
$C_{12}H_{18}O_5$	242.26	24.35	4	1.51599
$C_{12}H_{22}O_5$	246.29	25.03	2	1.45173
$C_{12}H_{21}O_5$	245.28	24.86	2.5	1.46723
$C_{12}H_{20}O_5$	244.27	24.69	3	1.48384

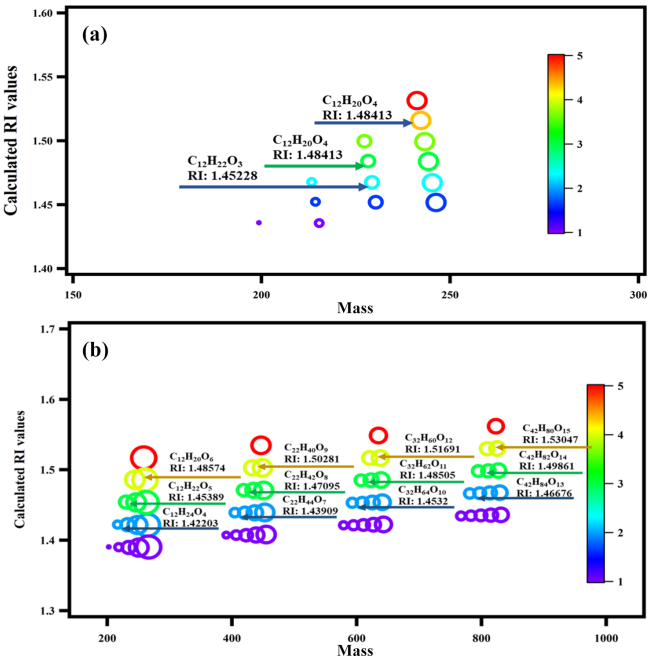

Figure 6. Calculated RI values of the surrogate system: **(a)** furan derivatives via intramolecular reaction, and **(b)** the oligomers via the formation of peroxyhemiacetal. The color map refers to the unsaturation of the molecular formula. The size of the circles indicates the size of the O/C ratio.

composition of *n*-dodecane SOA, we chose a surrogate system containing 11 PHA oligomerization and 2 cyclization reactions (with different degrees of unsaturation and different functional groups) to calculate the expected RI values using the quantitative structure–property relationship (QSPR) method based on the molecular formula and structure (Redmond and Thompson, 2011). The details of the 13 reactions and the related molecular information are shown in Fig. S3 in the Supplement and in Table 2; the relationship between the predicted RI values and the degree of unsaturation as well as the relationship between the predicted RI values and the degree of oligomerization are shown in Fig. 6. Strong correlations were observed between the predicted RI values and unsaturation and between the RI values and the degree of oligomerization. With the same unsaturation, the RI values increased with an increasing degree of oligomerization; under the same degree of oligomerization, the RI values increased with an increasing degree of unsaturation. In addition, the RI values of the surrogate system were similar to the identified substances, which further confirmed the effect of oligomers on RI values.

In addition to the abovementioned oligomer reasons, the difference in wall losses and gas–particle partitioning of gas-phase products might partially contribute to the RI enhancement under low-temperature conditions. The particle wall loss rates under both room and low-temperature conditions were measured. The wall loss rate under low-temperature

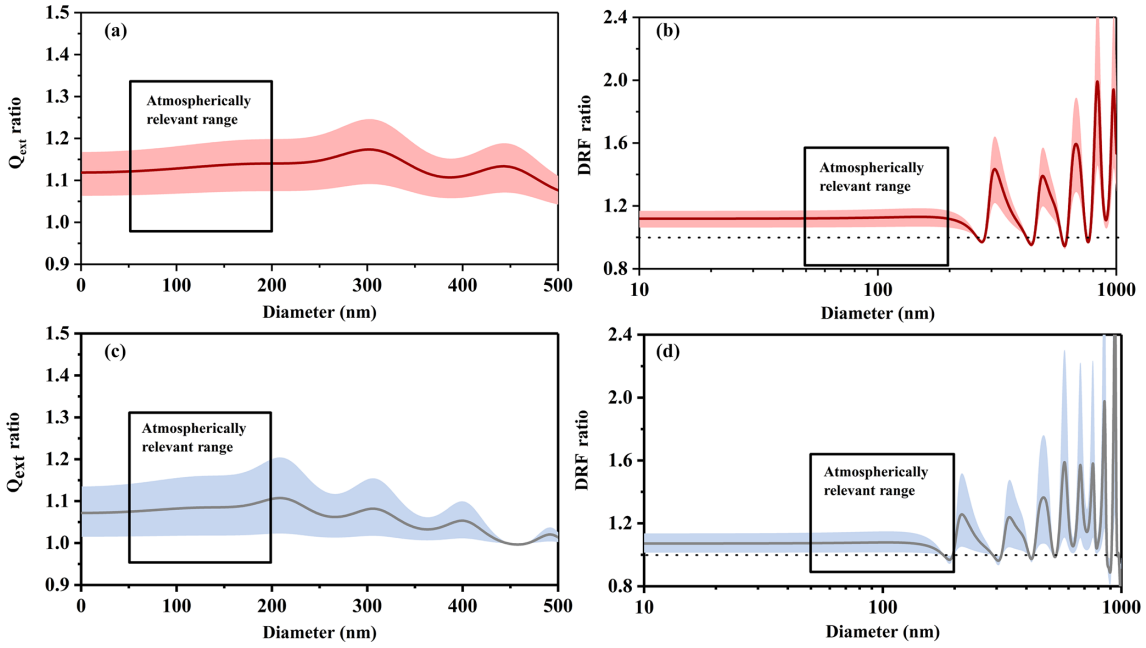

Figure 7. The light extinction efficiency ratio (Q_{ext} ratio) and the direct radiative forcing ratio (DRF ratio) of *n*-dodecane SOA under different temperature conditions. **(a)** Q_{ext} ratio at 532 nm; **(b)** DRF ratio at 532 nm; **(c)** Q_{ext} ratio at 375 nm; **(d)** DRF ratio at 375 nm. The solid line represents the average value of the ratio, and the shaded area represents the uncertainty.

conditions (0.0025–0.0028 min^{-1}) was larger than that at room temperature (0.0018–0.0020 min^{-1}). After wall loss correction, the SOA mass under low-temperature conditions was higher than that at room temperature. However, this difference in the particle wall loss rate can only slightly change the SOA mass concentration, and it cannot change the particle chemical composition; therefore, it is unlikely to change the optical properties. Nevertheless, the difference in the vapor wall loss rates may change the particle composition and optical properties. Low temperature can enhance the loss rates of higher-volatility compounds (whereas the dominant fate of lower-volatility compounds is condensation, so temperature may have little impact on their losses), which may lead to their lower proportions in SOA particles. As their RI values are generally lower than lower-volatility compounds (Li et al., 2018), this proportion change could enhance SOA RI at low temperature. Therefore, the difference in wall losses and gas–particle partitioning of gas-phase products might partially contribute to the RI enhancement under low-temperature conditions.

3.5 Atmospheric and climate implications

Figure 7 shows the light extinction efficiency (Q_{ext}) ratios and direct radiative forcing (DRF) ratios of *n*-dodecane SOA under different temperature conditions, from which we could establish the impacts of temperature on the role of *n*-dodecane SOA in visibility and radiative balance. As shown in Fig. 7a and c, the extinction efficiency (Q_{ext}) of SOA generated under low-temperature conditions is higher than for SOA generated at room temperature in the size range from 50 to 200 nm, which is the most atmospherically relevant size range (Zhang et al., 2015; Guo et al., 2014). The enhancement is about 7 %–20 % at 532 nm and about 1 %–21 % at 375 nm. This suggests that the extinction efficiency (Q_{ext}) of SOA formed from *n*-dodecane (and perhaps other long-chain alkanes in general) was higher in winter than in summer, which would result in lower visibility.

The enhancement in the light extinction of SOA and the oligomer compositions formed under low-temperature conditions might provide some possible insight into regional visibility issues, especially in suburban areas. It has been reported that UV-scattering particles in the boundary layer could accelerate photochemical reactions and haze production (Sun et al., 2014). The observations above showed that the scattering property of formed SOA increased under low-temperature conditions, which might provide one possible reason for the rapid occurrence of haze in suburban areas in winter. According to field observations, haze frequently occurs in winter, especially in China (Cheng et al., 2016; Huang et al., 2014; Guo et al., 2014; Parrish et al., 2007). When haze occurs, it is often accompanied by high-NO_x conditions, especially in urban areas. The temperature effects under high-NO_x conditions are also important and need to be investigated in future studies.

As shown in Fig. 7b and d, the DRF values under low-temperature conditions were generally larger than at room temperature: the enhancement was about 6 %–19 % at

532 nm (50–200 nm) and about 7 %–22 % at 375 nm (50–180 nm); for the 180–200 nm size range, low-temperature conditions decreased the DRF ratio by about 3 % at 375 nm. This phenomenon implies that the SOA generated in winter (low temperatures) might have larger direct radiative forcing effects on the Earth's surface than the SOA generated in summer (room temperature). It may also imply that temperature conditions should be considered when evaluating the DRF of the aerosol particles generated in the atmosphere.

4 Conclusions

To the best of our knowledge, this was the first report on the optical properties of long-chain alkane SOA under low-temperature conditions. The modification of temperature significantly changed the chemical composition of the particulate phase. From the oligomer component at low-temperature conditions, it was presumed that oligomerization was dominant at low temperatures. The presence of oligomers in the SOA particles resulted in an increase in the RI values. This study helps to improve our understanding of reduced visibility and the formation of haze in winter. Our results also show the need for further investigation of the atmospheric parameters influencing SOA formation and optical properties.

Data availability. The data used in this study are available upon request from the corresponding author.

Supplement. The supplement related to this article is available online at: https://doi.org/10.5194/acp-20-8123-2020-supplement.

Author contributions. WW conceived and led the studies. JL, WZ and CP performed chamber simulation and data analysis. KL, LZ, BS, YC, ML, HL and MG discussed the results and commented on the paper. JL prepared the article with contributions from all co-authors.

Competing interests. The authors declare that they have no conflict of interest.

Acknowledgements. This project was supported by the National Key Research and Development Program of China (grant no. 2017YFC0209506) and National Natural Science Foundation of China (grant nos. 41822703, 91744204 and 91844301).

Financial support. This research has been supported by the National Key Research and Development Program of China (grant no. 2017YFC0209506) and the National Natural Science Foundation of China (grant nos. 41822703, 91744204, and 91844301).

Review statement. This paper was edited by Alex Lee and reviewed by two anonymous referees.

References

Aimanant, S. and Ziemann, P. J.: Chemical mechanisms of aging of aerosol formed from the reaction of n-pentadecane with OH radicals in the presence of NO_x, Aerosol Sci. Tech., 47, 979–990, https://doi.org/10.1080/02786826.2013.804621, 2013.

Atkinson, R. and Arey, J.: Atmospheric degradation of volatile organic compounds, Chem. Rev., 103, 4605–4638, https://doi.org/10.1021/cr0206420, 2003.

Bohren, C. F. and Huffman, D. R.: Absorption and Scattering of Light by Small Particles, Wiley VCH, 1983.

Bond, T. C. and Bergstrom, R. W.: Light absorption by carbonaceous particles: An investigative review, Aerosol Sci. Tech., 40, 27–67, https://doi.org/10.1080/02786820500421521, 2006.

Boyd, C. M., Nah, T., Xu, L., Berkemeier, T., and Ng, N. L.: Secondary organic aerosol (SOA) from nitrate radical oxidation of monoterpenes: Effects of temperature, dilution, and humidity on aerosol formation, mixing, and evaporation, Environ. Sci. Technol., 51, 7831–7841, https://doi.org/10.1021/acs.est.7b01460, 2017.

Cappa, C. D., Che, D. L., Kessler, S. H., Kroll, J. H., and Wilson, K. R.: Variations in organic aerosol optical and hygroscopic properties upon heterogeneous OH oxidation, J. Geophys. Res., 116, D15204, https://doi.org/10.1029/2011jd015918, 2011.

Charron, A., Polo-Rehn, L., Besombes, J.-L., Golly, B., Buisson, C., Chanut, H., Marchand, N., Guillaud, G., and Jaffrezo, J.-L.: Identification and quantification of particulate tracers of exhaust and non-exhaust vehicle emissions, Atmos. Chem. Phys., 19, 5187–5207, https://doi.org/10.5194/acp-19-5187-2019, 2019.

Cheng, Y., Zheng, G., Wei, C., Mu, Q., Zheng, B., Wang, Z., Gao, M., Zhang, Q., He, K., Carmichael, G., Poschl, U., and Su, H.: Reactive nitrogen chemistry in aerosol water as a source of sulfate during haze events in China, Sci. Adv., 2, e1601530, https://doi.org/10.1126/sciadv.1601530, 2016.

Clark, C. H., Kacarab, M., Nakao, S., Asa-Awuku, A., Sato, K., and Cocker III, D. R.: Temperature effects on secondary organic aerosol (SOA) from the dark ozonolysis and photo-oxidation of isoprene, Environ. Sci. Technol., 50, 5564–5571, https://doi.org/10.1021/acs.est.5b05524, 2016.

Cui, L., Zhang, Z., Huang, Y., Lee, S. C., Blake, D. R., Ho, K. F., Wang, B., Gao, Y., Wang, X. M., and Louie, P. K. K.: Measuring OVOCs and VOCs by PTR-MS in an urban roadside microenvironment of Hong Kong: relative humidity and temperature dependence, and field intercomparisons, Atmos. Meas. Tech., 9, 5763–5779, https://doi.org/10.5194/amt-9-5763-2016, 2016.

Denjean, C., Formenti, P., Picquet-Varrault, B., Katrib, Y., Pangui, E., Zapf, P., and Doussin, J. F.: A new experimental approach to study the hygroscopic and optical properties of aerosols: application to ammonium sulfate particles, Atmos. Meas. Tech., 7, 183–197, https://doi.org/10.5194/amt-7-183-2014, 2014.

Denjean, C., Formenti, P., Picquet-Varrault, B., Pangui, E., Zapf, P., Katrib, Y., Giorio, C., Tapparo, A., Monod, A., Temime-Roussel, B., Decorse, P., Mangeney, C., and Doussin, J. F.: Relating hygroscopicity and optical properties to chemical composition and structure of secondary organic aerosol particles generated from

the ozonolysis of α-pinene, Atmos. Chem. Phys., 15, 3339–3358, https://doi.org/10.5194/acp-15-3339-2015, 2015.

Ding, X., Zhang, Y. Q., He, Q. F., Yu, Q. Q., Wang, J. Q., Shen, R. Q., Song, W., Wang, Y. S., and Wang, X. M.: Significant increase of aromatics-derived secondary organic aerosol during fall to winter in China, Environ. Sci. Technol., 51, 7432–7441, https://doi.org/10.1021/acs.est.6b06408, 2017.

Emanuelsson, E. U., Watne, A. K., Lutz, A., Ljungstrom, E., and Hallquist, M.: Influence of humidity, temperature, and radicals on the formation and thermal properties of secondary organic aerosol (SOA) from ozonolysis of beta-pinene, J. Phys. Chem. A, 117, 10346–10358, https://doi.org/10.1021/jp4010218, 2013.

Ervens, B., Turpin, B. J., and Weber, R. J.: Secondary organic aerosol formation in cloud droplets and aqueous particles (aq-SOA): a review of laboratory, field and model studies, Atmos. Chem. Phys., 11, 11069–11102, https://doi.org/10.5194/acp-11-11069-2011, 2011.

Fahnestock, K. A. S., Yee, L. D., Loza, C. L., Coggon, M. M., Schwantes, R., Zhang, X., Dalleska, N. F., and Seinfeld, J. H.: Secondary organic aerosol composition from C-12 Alkanes, J. Phys. Chem. A, 119, 4281–4297, https://doi.org/10.1021/jp501779w, 2015.

Flores, J. M., Washenfelder, R. A., Adler, G., Lee, H. J., Segev, L., Laskin, J., Laskin, A., Nizkorodov, S. A., Brown, S. S., and Rudich, Y.: Complex refractive indices in the near-ultraviolet spectral region of biogenic secondary organic aerosol aged with ammonia, Phys. Chem. Chem. Phys., 16, 10629–10642, https://doi.org/10.1039/c4cp01009d, 2014.

Gentner, D. R., Isaacman, G., Worton, D. R., Chan, A. W. H., Dallmann, T. R., Davis, L., Liu, S., Day, D. A., Russell, L. M., Wilson, K. R., Weber, R., Guha, A., Harley, R. A., and Goldstein, A. H.: Elucidating secondary organic aerosol from diesel and gasoline vehicles through detailed characterization of organic carbon emissions, P. Natl. Acad. Sci. USA, 109, 18318–18323, https://doi.org/10.1073/pnas.1212272109, 2012.

Gentner, D. R., Jathar, S. H., Gordon, T. D., Bahreini, R., Day, D. A., El Haddad, I., Hayes, P. L., Pieber, S. M., Platt, S. M., de Gouw, J., Goldstein, A. H., Harley, R. A., Jimenez, J. L., Prévôt, A. S. H., and Robinson, A. L.: Review of urban secondary organic aerosol formation from gasoline and diesel motor vehicle emissions, Environ. Sci. Technol., 51, 1074–1093, https://doi.org/10.1021/acs.est.6b04509, 2017.

George, C., Ammann, M., D'Anna, B., Donaldson, D. J., and Nizkorodov, S. A.: Heterogeneous photochemistry in the atmosphere, Chem. Rev., 115, 4218–4258, https://doi.org/10.1021/cr500648z, 2015.

Girolami, G. S.: A simple "back of the envelope" method for estimating the densities and molecular volumes of liquids and solids, J. Chem. Educ., 71, 962–964, 1994.

Guo, S., Hu, M., Zamora, M. L., Peng, J., Shang, D., Zheng, J., Du, Z., Wu, Z., Shao, M., Zeng, L., Molina, M. J., and Zhang, R.: Elucidating severe urban haze formation in China, P. Natl. Acad. Sci. USA, 111, 17373–17378, https://doi.org/10.1073/pnas.1419604111, 2014.

Hallquist, M., Wenger, J. C., Baltensperger, U., Rudich, Y., Simpson, D., Claeys, M., Dommen, J., Donahue, N. M., George, C., Goldstein, A. H., Hamilton, J. F., Herrmann, H., Hoffmann, T., Iinuma, Y., Jang, M., Jenkin, M. E., Jimenez, J. L., Kiendler-Scharr, A., Maenhaut, W., McFiggans, G., Mentel, Th. F., Monod, A., Prévôt, A. S. H., Seinfeld, J. H., Surratt, J. D., Szmigielski, R., and Wildt, J.: The formation, properties and impact of secondary organic aerosol: current and emerging issues, Atmos. Chem. Phys., 9, 5155–5236, https://doi.org/10.5194/acp-9-5155-2009, 2009.

Huang, M., Hao, L., Cai, S., Gu, X., Zhang, W., Hu, C., Wang, Z., Fang, L., and Zhang, W.: Effects of inorganic seed aerosols on the particulate products of aged 1,3,5-trimethylbenzene secondary organic aerosol, Atmos. Environ., 152, 490–502, https://doi.org/10.1016/j.atmosenv.2017.01.010, 2017.

Huang, R. J., Zhang, Y., Bozzetti, C., Ho, K. F., Cao, J. J., Han, Y., Daellenbach, K. R., Slowik, J. G., Platt, S. M., Canonaco, F., Zotter, P., Wolf, R., Pieber, S. M., Bruns, E. A., Crippa, M., Ciarelli, G., Piazzalunga, A., Schwikowski, M., Abbaszade, G., Schnelle-Kreis, J., Zimmermann, R., An, Z., Szidat, S., Baltensperger, U., El Haddad, I., and Prevot, A. S.: High secondary aerosol contribution to particulate pollution during haze events in China, Nature, 514, 218–222, https://doi.org/10.1038/nature13774, 2014.

Huang, W., Saathoff, H., Pajunoja, A., Shen, X., Naumann, K.-H., Wagner, R., Virtanen, A., Leisner, T., and Mohr, C.: α-Pinene secondary organic aerosol at low temperature: chemical composition and implications for particle viscosity, Atmos. Chem. Phys., 18, 2883–2898, https://doi.org/10.5194/acp-18-2883-2018, 2018.

Hunter, J. F., Carrasquillo, A. J., Daumit, K. E., and Kroll, J. H.: Secondary organic aerosol formation from acyclic, monocyclic, and polycyclic alkanes, Environ. Sci. Technol., 48, 10227–10234, https://doi.org/10.1021/es502674s, 2014.

Kanakidou, M., Seinfeld, J. H., Pandis, S. N., Barnes, I., Dentener, F. J., Facchini, M. C., Van Dingenen, R., Ervens, B., Nenes, A., Nielsen, C. J., Swietlicki, E., Putaud, J. P., Balkanski, Y., Fuzzi, S., Horth, J., Moortgat, G. K., Winterhalter, R., Myhre, C. E. L., Tsigaridis, K., Vignati, E., Stephanou, E. G., and Wilson, J.: Organic aerosol and global climate modelling: a review, Atmos. Chem. Phys., 5, 1053–1123, https://doi.org/10.5194/acp-5-1053-2005, 2005.

Kim, H. and Paulson, S. E.: Real refractive indices and volatility of secondary organic aerosol generated from photooxidation and ozonolysis of limonene, α-pinene and toluene, Atmos. Chem. Phys., 13, 7711–7723, https://doi.org/10.5194/acp-13-7711-2013, 2013.

Kim, H., Liu, S., Russell, L. M., and Paulson, S. E.: Dependence of real refractive indices on O : C, H : C and mass fragments of secondary organic aerosol generated from ozonolysis and photooxidation of limonene and alpha-pinene, Aerosol Sci. Technol., 48, 498–507, https://doi.org/10.1080/02786826.2014.893278, 2014.

Koss, A. R., Warneke, C., Yuan, B., Coggon, M. M., Veres, P. R., and de Gouw, J. A.: Evaluation of NO^+ reagent ion chemistry for online measurements of atmospheric volatile organic compounds, Atmos. Meas. Tech., 9, 2909–2925, https://doi.org/10.5194/amt-9-2909-2016, 2016.

Lambe, A. T., Onasch, T. B., Croasdale, D. R., Wright, J. P., Martin, A. T., Franklin, J. P., Massoli, P., Kroll, J. H., Canagaratna, M. R., Brune, W. H., Worsnop, D. R., and Davidovits, P.: Transitions from functionalization to fragmentation reactions of laboratory secondary organic aerosol (SOA) generated from the OH oxidation of alkane precursors, Environ. Sci. Technol., 46, 5430–5437, https://doi.org/10.1021/es300274t, 2012.

Lambe, A. T., Cappa, C. D., Massoli, P., Onasch, T. B., Forestieri, S. D., Martin, A. T., Cummings, M. J., Croasdale, D. R., Brune, W. H., Worsnop, D. R., and Davidovits, P.: Relationship between oxidation level and optical properties of secondary organic aerosol, Environ. Sci. Technol., 47, 6349–6357, https://doi.org/10.1021/es401043j, 2013.

Lambe, A. T., Chhabra, P. S., Onasch, T. B., Brune, W. H., Hunter, J. F., Kroll, J. H., Cummings, M. J., Brogan, J. F., Parmar, Y., Worsnop, D. R., Kolb, C. E., and Davidovits, P.: Effect of oxidant concentration, exposure time, and seed particles on secondary organic aerosol chemical composition and yield, Atmos. Chem. Phys., 15, 3063–3075, https://doi.org/10.5194/acp-15-3063-2015, 2015.

Lamkaddam, H., Gratien, A., Pangui, E., Cazaunau, M., Picquet-Varrault, B., and Doussin, J.-F.: High-NO_x photooxidation of n-dodecane: Temperature dependence of SOA formation, Environ. Sci. Technol., 51, 192–201, https://doi.org/10.1021/acs.est.6b03821, 2016.

Laskin, A., Laskin, J., and Nizkorodov, S. A.: Chemistry of atmospheric brown carbon, Chem. Rev., 115, 4335–4382, https://doi.org/10.1021/cr5006167, 2015.

Lee, A. K. Y., Zhao, R., Li, R., Liggio, J., Li, S.-M., and Abbatt, J. P. D.: Formation of light absorbing organo-nitrogen species from evaporation of droplets containing glyoxal and ammonium sulfate, Environ. Sci. Technol., 47, 12819–12826, https://doi.org/10.1021/es402687w, 2013.

Li, K., Wang, W., Ge, M., Li, J., and Wang, D.: Optical properties of secondary organic aerosols generated by photooxidation of aromatic hydrocarbons, Sci. Rep., 4, 4922–4922, https://doi.org/10.1038/srep04922, 2014.

Li, J., Li, K., Wang, W., Wang, J., Peng, C., and Ge, M.: Optical properties of secondary organic aerosols derived from long-chain alkanes under various NO_x and seed conditions, Sci. Total Environ., 579, 1699–1705, https://doi.org/10.1016/j.scitotenv.2016.11.189, 2017a.

Li, K., Li, J., Liggio, J., Wang, W., Ge, M., Liu, Q., Guo, Y., Tong, S., Li, J., Peng, C., Jing, B., Wang, D., and Fu, P.: Enhanced light scattering of secondary organic aerosols by multiphase reactions, Environ. Sci. Technol., 51, 1285–1292, https://doi.org/10.1021/acs.est.6b03229, 2017b.

Li, K., Li, J., Wang, W., Li, J., Peng, C., Wang, D., and Ge, M.: Effects of gas-particle partitioning on refractive index and chemical composition of m-xylene secondary organic aerosol, J. Phys. Chem. A, 122, 3250–3260, https://doi.org/10.1021/acs.jpca.7b12792, 2018.

Li, J., Wang, W., Li, K., Zhang, W., Ge, M., and Peng, C.: Development and application of the multi-wavelength cavity ring-down aerosol extinction spectrometer, J. Environ. Sci. (China), 76, 227–237, https://doi.org/10.1016/j.jes.2018.04.030, 2019.

Lim, Y. B. and Ziemann, P. J.: Products and mechanism of secondary organic aerosol formation from reactions of n-alkanes with OH radicals in the presence of NO_x, Environ. Sci. Technol., 39, 9229–9236, https://doi.org/10.1021/es051447g, 2005.

Lim, Y. B. and Ziemann, P. J.: Effects of molecular structure on aerosol yields from OH radical-initiated reactions of linear, branched, and cyclic alkanes in the presence of NO_x, Environ. Sci. Technol., 43, 2328–2334, https://doi.org/10.1021/es803389s, 2009a.

Lim, Y. B. and Ziemann, P. J.: Chemistry of secondary organic aerosol formation from OH radical-initiated reactions of linear, branched, and cyclic alkanes in the presence of NO_x, Aerosol Sci. Tech., 43, 604–619, https://doi.org/10.1080/02786820902802567, 2009b.

Lin, P., Liu, J., Shilling, J. E., Kathmann, S. M., Laskin, J., and Laskin, A.: Molecular characterization of brown carbon (BrC) chromophores in secondary organic aerosol generated from photo-oxidation of toluene, Phys. Chem. Chem. Phys., 17, 23312–23325, https://doi.org/10.1039/c5cp02563j, 2015.

Liu, H., Man, H., Cui, H., Wang, Y., Deng, F., Wang, Y., Yang, X., Xiao, Q., Zhang, Q., Ding, Y., and He, K.: An updated emission inventory of vehicular VOCs and IVOCs in China, Atmos. Chem. Phys., 17, 12709–12724, https://doi.org/10.5194/acp-17-12709-2017, 2017.

Liu, P. F., Abdelmalki, N., Hung, H.-M., Wang, Y., Brune, W. H., and Martin, S. T.: Ultraviolet and visible complex refractive indices of secondary organic material produced by photooxidation of the aromatic compounds toluene and *m*-xylene, Atmos. Chem. Phys., 15, 1435–1446, https://doi.org/10.5194/acp-15-1435-2015, 2015.

Loza, C. L., Craven, J. S., Yee, L. D., Coggon, M. M., Schwantes, R. H., Shiraiwa, M., Zhang, X., Schilling, K. A., Ng, N. L., Canagaratna, M. R., Ziemann, P. J., Flagan, R. C., and Seinfeld, J. H.: Secondary organic aerosol yields of 12-carbon alkanes, Atmos. Chem. Phys., 14, 1423–1439, https://doi.org/10.5194/acp-14-1423-2014, 2014.

Lu, J. W., Flores, J. M., Lavi, A., Abo-Riziq, A., and Rudich, Y.: Changes in the optical properties of benzo a pyrene-coated aerosols upon heterogeneous reactions with NO_2 and NO_3, Phys. Chem. Chem. Phys., 13, 6484–6492, https://doi.org/10.1039/c0cp02114h, 2011.

Lu, K., Guo, S., Tan, Z., Wang, H., Shang, D., Liu, Y., Li, X., Wu, Z., Hu, M., and Zhang, Y.: Exploring atmospheric free-radical chemistry in China: the self-cleansing capacity and the formation of secondary air pollution, Natl. Sci. Rev., 6, 579–594, https://doi.org/10.1093/nsr/nwy073, 2018.

McNeill, V. F.: Aqueous organic chemistry in the atmosphere: sources and chemical processing of organic aerosols, Environ. Sci. Technol., 49, 1237–1244, https://doi.org/10.1021/es5043707, 2015.

Mellouki, A., Wallington, T. J., and Chen, J.: Atmospheric chemistry of oxygenated volatile organic compounds: impacts on air quality and climate, Chem. Rev., 115, 3984–4014, https://doi.org/10.1021/cr500549n, 2015.

Michel Flores, J., Bar-Or, R. Z., Bluvshtein, N., Abo-Riziq, A., Kostinski, A., Borrmann, S., Koren, I., Koren, I., and Rudich, Y.: Absorbing aerosols at high relative humidity: linking hygroscopic growth to optical properties, Atmos. Chem. Phys., 12, 5511–5521, https://doi.org/10.5194/acp-12-5511-2012, 2012.

Moise, T., Flores, J. M., and Rudich, Y.: Optical properties of secondary organic aerosols and their changes by chemical processes, Chem. Rev., 115, 4400–4439, https://doi.org/10.1021/cr5005259, 2015.

Mu, Q., Shiraiwa, M., Octaviani, M., Ma, N., Ding, A., Su, H., Lammel, G., Pöschl, U., and Cheng, Y.: Temperature effect on phase state and reactivity controls atmospheric multiphase chemistry and transport of PAHs, Sci. Adv., 4, eaap7314, https://doi.org/10.1126/sciadv.aap7314, 2018.

Nakayama, T., Matsumi, Y., Sato, K., Imamura, T., Yamazaki, A., and Uchiyama, A.: Laboratory studies on optical properties of secondary organic aerosols generated during the photooxidation of toluene and the ozonolysis of α-pinene, J. Geophys. Res., 115, D24204, https://doi.org/10.1029/2010jd014387, 2010.

Nakayama, T., Sato, K., Matsumi, Y., Imamura, T., Yamazaki, A., and Uchiyama, A.: Wavelength and NO_x dependent complex refractive index of SOAs generated from the photooxidation of toluene, Atmos. Chem. Phys., 13, 531–545, https://doi.org/10.5194/acp-13-531-2013, 2013.

Parrish, D. D., Stohl, A., Forster, C., Atlas, E. L., Blake, D. R., Goldan, P. D., Kuster, W. C., and de Gouw, J. A.: Effects of mixing on evolution of hydrocarbon ratios in the troposphere, J. Geophys. Res.-Atmos., 112, D10S34, https://doi.org/10.1029/2006jd007583, 2007.

Paulsen, D., Dommen, J., Kalberer, M., Preavot, A. S. H., Richter, R., Sax, M., Steinbacher, M., Weingartner, E., and Baltensperger, U.: Secondary organic aerosol formation by irradiation of 1,3,5-trimethylbenzene-NO_x-H_2O in a new reaction chamber for atmospheric chemistry and physics, Environ. Sci. Technol., 39, 2668–2678, 2005.

Peng, C., Wang, W., Li, K., Li, J., Zhou, L., Wang, L., and Ge, M.: The optical properties of limonene secondary organic aerosols: the role of NO_3, OH and O_3 in the oxidation processes, J. Geophys. Res.-Atmos., 123, 3292–3303, https://doi.org/10.1002/2017jd028090, 2018.

Phillips, S. M. and Smith, G. D.: Light absorption by charge transfer complexes in brown carbon aerosols, Environ. Sci. Tech. Let., 1, 382–386, https://doi.org/10.1021/ez500263j, 2014.

Pöschl, U.: Atmospheric aerosols: Composition, transformation, climate and health effects, Angew. Chem.-Int. Edit., 44, 7520–7540, https://doi.org/10.1002/anie.200501122, 2005.

Poschl, U. and Shiraiwa, M.: Multiphase chemistry at the atmosphere-biosphere interface influencing climate and public health in the anthropocene, Chem. Rev., 115, 4440–4475, https://doi.org/10.1021/cr500487s, 2015.

Presto, A. A., Miracolo, M. A., Kroll, J. H., Worsnop, D. R., Robinson, A. L., and Donahue, N. M.: Intermediate-volatility organic compounds: A potential source of ambient oxidized organic aerosol, Environ. Sci. Technol., 43, 4744–4749, https://doi.org/10.1021/es803219q, 2009.

Price, D. J., Kacarab, M., Cocker, D. R., Purvis-Roberts, K. L., and Silva, P. J.: Effects of temperature on the formation of secondary organic aerosol from amine precursors, Aerosol Sci. Technol., 50, 1216–1226, https://doi.org/10.1080/02786826.2016.1236182, 2016.

Qi, L., Nakao, S., Tang, P., and Cocker III, D. R.: Temperature effect on physical and chemical properties of secondary organic aerosol from *m*-xylene photooxidation, Atmos. Chem. Phys., 10, 3847–3854, https://doi.org/10.5194/acp-10-3847-2010, 2010.

Redmond, H. and Thompson, J. E.: Evaluation of a quantitative structure-property relationship (QSPR) for predicting mid-visible refractive index of secondary organic aerosol (SOA), Phys. Chem. Chem. Phys., 13, 6872–6882, https://doi.org/10.1039/c0cp02270e, 2011.

Roy, A. and Choi, Y.: Effect of ambient temperature on species lumping for total organic gases in gasoline exhaust emissions, Atmos. Environ., 152, 240–245, https://doi.org/10.1016/j.atmosenv.2016.11.057, 2017.

Sareen, N., Waxman, E. M., Turpin, B. J., Volkamer, R., and Carlton, A. G.: Potential of aerosol liquid water to facilitate organic aerosol formation: Assessing knowledge gaps about precursors and partitioning, Environ. Sci. Technol., 51, 3327–3335, https://doi.org/10.1021/acs.est.6b04540, 2017.

Shi, B., Wang, W., Zhou, L., Sun, Z., Fan, C., Chen, Y., Zhang, W., Qiao, Y., Qiao, Y., and Ge, M.: Atmospheric oxidation of $C_{10\sim14}$ *n*-alkanes initiated by Cl atoms: Kinetics and mechanism, Atmos. Environ., 222, 117166, https://doi.org/10.1016/j.atmosenv.2019.117166, 2019.

Shrivastava, M., Cappa, C. D., Fan, J., Goldstein, A. H., Guenther, A. B., Jimenez, J. L., Kuang, C., Laskin, A., Martin, S. T., Ng, N. L., Petaja, T., Pierce, J. R., Rasch, P. J., Roldin, P., Seinfeld, J. H., Shilling, J., Smith, J. N., Thornton, J. A., Volkamer, R., Wang, J., Worsnop, D. R., Zaveri, R. A., Zelenyuk, A., and Zhang, Q.: Recent advances in understanding secondary organic aerosol: Implications for global climate forcing, Rev. Geophys., 55, 509–559, https://doi.org/10.1002/2016rg000540, 2017.

Song, C., Gyawali, M., Zaveri, R. A., Shilling, J. E., and Arnott, W. P.: Light absorption by secondary organic aerosol from alpha-pinene: Effects of oxidants, seed aerosol acidity, and relative humidity, J. Geophys. Res.-Atmos., 118, 11741–11749, https://doi.org/10.1002/jgrd.50767, 2013.

Sun, Y., Jiang, Q., Wang, Z., Fu, P., Li, J., Yang, T., and Yin, Y.: Investigation of the sources and evolution processes of severe haze pollution in Beijing in January 2013, J. Geophys. Res.-Atmos., 119, 4380–4398, https://doi.org/10.1002/2014jd021641, 2014.

Svendby, T. M., Lazaridis, M., and Tørseth, K.: Temperature dependent secondary organic aerosol formation from terpenes and aromatics, J. Atmos. Chem., 59, 25–46, https://doi.org/10.1007/s10874-007-9093-7, 2008.

Takekawa, H., Minoura, H., and Yamazaki, S.: Temperature dependence of secondary organic aerosol formation by photooxidation of hydrocarbons, Atmos. Environ., 37, 3413–3424, https://doi.org/10.1016/s1352-2310(03)00359-5, 2003.

Titos, G., Cazorla, A., Zieger, P., Andrews, E., Lyamani, H., Granados-Muñoz, M. J., Olmo, F. J., and Alados-Arboledas, L.: Effect of hygroscopic growth on the aerosol light-scattering coefficient: A review of measurements, techniques and error sources, Atmos. Environ., 141, 494–507, https://doi.org/10.1016/j.atmosenv.2016.07.021, 2016.

Trainic, M., Abo Riziq, A., Lavi, A., Flores, J. M., and Rudich, Y.: The optical, physical and chemical properties of the products of glyoxal uptake on ammonium sulfate seed aerosols, Atmos. Chem. Phys., 11, 9697–9707, https://doi.org/10.5194/acp-11-9697-2011, 2011.

von Schneidemesser, E., Monks, P. S., Allan, J. D., Bruhwiler, L., Forster, P., Fowler, D., Lauer, A., Morgan, W. T., Paasonen, P., Righi, M., Sindelarova, K., and Sutton, M. A.: Chemistry and the linkages between air quality and climate change, Chem. Rev., 115, 3856–3897, https://doi.org/10.1021/acs.chemrev.5b00089, 2015.

Wang, J. M., Jeong, C.-H., Zimmerman, N., Healy, R. M., Hilker, N., and Evans, G. J.: Real-world emission of particles from vehicles: Volatility and the effects of ambient temperature, Environ. Sci. Technol., 51, 4081–4090, https://doi.org/10.1021/acs.est.6b05328, 2017.

Wang, L., Wang, W., and Ge, M.: Extinction efficiencies of mixed aerosols measured by aerosol cavity ring

down spectrometry, Chinese Sci. Bull., 57, 2567–2573, https://doi.org/10.1007/s11434-012-5146-7, 2012.

Wang, W.-G., Li, K., Zhou, L., Ge, M.-F., Hou, S.-Q., Tong, S.-R., Mu, Y.-J., and Jia, L.: Evaluation and application of dual-reactor chamber for studying atmospheric oxidation processes and mechanisms, Acta Phys.-Chim. Sin., 31, 1251–1259, https://doi.org/10.3866/pku.whxb201504161, 2015.

Warren, B., Austin, R. L., and Cocker, D. R.: Temperature dependence of secondary organic aerosol, Atmos. Environ., 43, 3548–3555, https://doi.org/10.1016/j.atmosenv.2009.04.011, 2009.

Ye, Q., Robinson, E. S., Ding, X., Ye, P., Sullivan, R. C., and Donahue, N. M.: Mixing of secondary organic aerosols versus relative humidity, P. Natl. Acad. Sci. USA, 113, 12649–12654, https://doi.org/10.1073/pnas.1604536113, 2016.

Yee, L. D., Craven, J. S., Loza, C. L., Schilling, K. A., Ng, N. L., Canagaratna, M. R., Ziemann, P. J., Flagan, R. C., and Seinfeld, J. H.: Secondary organic aerosol formation from low-NO(x) photooxidation of dodecane: evolution of multigeneration gas-phase chemistry and aerosol composition, J. Phys. Chem. A, 116, 6211–6230, https://doi.org/10.1021/jp211531h, 2012.

Yee, L. D., Craven, J. S., Loza, C. L., Schilling, K. A., Ng, N. L., Canagaratna, M. R., Ziemann, P. J., Flagan, R. C., and Seinfeld, J. H.: Effect of chemical structure on secondary organic aerosol formation from C_{12} alkanes, Atmos. Chem. Phys., 13, 11121–11140, https://doi.org/10.5194/acp-13-11121-2013, 2013.

Zhang, R., Wang, G., Guo, S., Zamora, M. L., Ying, Q., Lin, Y., Wang, W., Hu, M., and Wang, Y.: Formation of urban fine particulate matter, Chem. Rev., 115, 3803–3855, https://doi.org/10.1021/acs.chemrev.5b00067, 2015.

Zhao, B., Wang, S., Donahue, N. M., Jathar, S. H., Huang, X., Wu, W., Hao, J., and Robinson, A. L.: Quantifying the effect of organic aerosol aging and intermediate-volatility emissions on regional-scale aerosol pollution in China, Sci. Rep., 6, 28815, https://doi.org/10.1038/srep28815, 2016.

Zhao, Y., Hennigan, C. J., May, A. A., Tkacik, D. S., de Gouw, J. A., Gilman, J. B., Kuster, W. C., Borbon, A., and Robinson, A. L.: Intermediate-volatility organic compounds: a large source of secondary organic aerosol, Environ. Sci. Technol., 48, 13743–13750, https://doi.org/10.1021/es5035188, 2014.

Zhao, Z., Le, C., Xu, Q., Peng, W., Jiang, H., Lin, Y.-H., Cocker, D. R., and Zhang, H.: Compositional evolution of secondary organic aerosol as temperature and relative humidity cycle in atmospherically relevant ranges, ACS Earth Space Chem., 3, 2549–2558, https://doi.org/10.1021/acsearthspacechem.9b00232, 2019.

Zhong, M. and Jang, M.: Dynamic light absorption of biomass-burning organic carbon photochemically aged under natural sunlight, Atmos. Chem. Phys., 14, 1517–1525, https://doi.org/10.5194/acp-14-1517-2014, 2014.